

# Electrochemical Based C-Reactive Protein (CRP) Sensing Through Molecularly Imprinted Polymer (MIP) Pore Structure Coupled with Bi-Metallic Tuned Screen-Printed Electrode

Sapna Balayan<sup>1</sup> , Nidhi Chauhan<sup>1</sup> , Ramesh Chandra<sup>2,\*</sup> , Utkarsh Jain<sup>1,\*</sup> 

<sup>1</sup> Amity Institute of Nanotechnology (AINT), Amity University Uttar Pradesh (AUUP), Sector -125, Noida- 201313, India; sbalayan@amity.edu (S.B.); nchauhan1@amity.edu (N.C.); ujain@amity.edu (U.J.);

<sup>2</sup> Drug Discovery and Development Laboratory, Department of Chemistry, University of Delhi, Delhi- 110007, INDIA; acbrdu@hotmail.com (R.C.);

\* Correspondence: ujain@amity.edu (U.J.), karshjain@gmail.com (U.J.); acbrdu@hotmail.com (R.C.);

Scopus Author ID 56534847500

Received: 17.09.2021; Revised: 1.11.2021; Accepted: 4.11.2021; Published: 28.11.2021

**Abstract:** Neonatal sepsis is a serious and potentially life-threatening condition and a major cause of higher mortality and morbidity in the infant population. At present, the available for neonatal sepsis detection is conventional microbial testing. However, this method has various constraints, including being expensive, requiring qualified individuals, large sample volume needed for testing, and time-consuming process. The emergence of biosensors facilitates advantages over these constraints. The presented work describes the development of an electrochemical biosensor detecting C-reactive protein, a biomarker for neonatal sepsis, utilizing molecularly imprinted polymer fabricated on an electrode surface. Gold-platinum bimetallic nanomaterials were coated on the screen-printed carbon electrode to enhance the sensor's surface area and catalytic property. The C-reactive protein imprinted polymer was then deposited on the surface of the electrode. Further, the electrochemical technique was applied to measure the response of the developed electrode. It was observed that the sensing matrix was able to detect C-reactive protein and can be operated in a wide detection range and exhibits a lower detection limit as 0.1 nM with higher sensitivity (0.14  $\mu\text{A/nM}$ ). The developed sensing platform can provide a user-friendly approach and rapid detection results.

**Keywords:** C-reactive protein; sepsis; neonatal; molecularly imprinted polymer.

© 2021 by the authors. This article is an open-access article distributed under the terms and conditions of the Creative Commons Attribution (CC BY) license (<https://creativecommons.org/licenses/by/4.0/>).

## 1. Introduction

Over the last decade, neonatal sepsis has been considered a prime cause of increased mortality and morbidity in the Intensive Care Units (ICU) for neonates [1-5]. About 15 % of neonates suffer from sepsis either in their early or late stages (Figure 1). The pathogens causing sepsis are *Klebsiella spp.*, Group B *streptococcus* (GBS), non-typhoidal *Escherichia coli* (*E. coli*), *Salmonella* bacteria, *Listeria monocytogenes*, *Staphylococcus aureus* (*S. aureus*), and *Haemophilus influenzae*. Neonatal sepsis can be manifested into two categories. Firstly, Early-onset neonatal sepsis occurs within 7 days of life, and then late-onset neonatal sepsis is developed within 90 days of life. About 1-2/1000 neonate lives are affected by EOS. On the other side, LOS refers to the disorders within 90 days after birth, and about 6/1000 lives are affected by LOS. The reported studies show that a higher infection rate is observed in Very-

low-birth-weight (VLBW) infants that is about 20 per 1000 lives for EOS, and for LOS it is 200 per 1000 lives [5-9]. It is quite difficult to diagnose neonatal sepsis early during routine clinical practices because its symptoms are similar to non-infectious disorders. Introducing accurate diagnostic testing may help record true sepsis cases and eliminate unnecessary use of antibiotics on neonates.

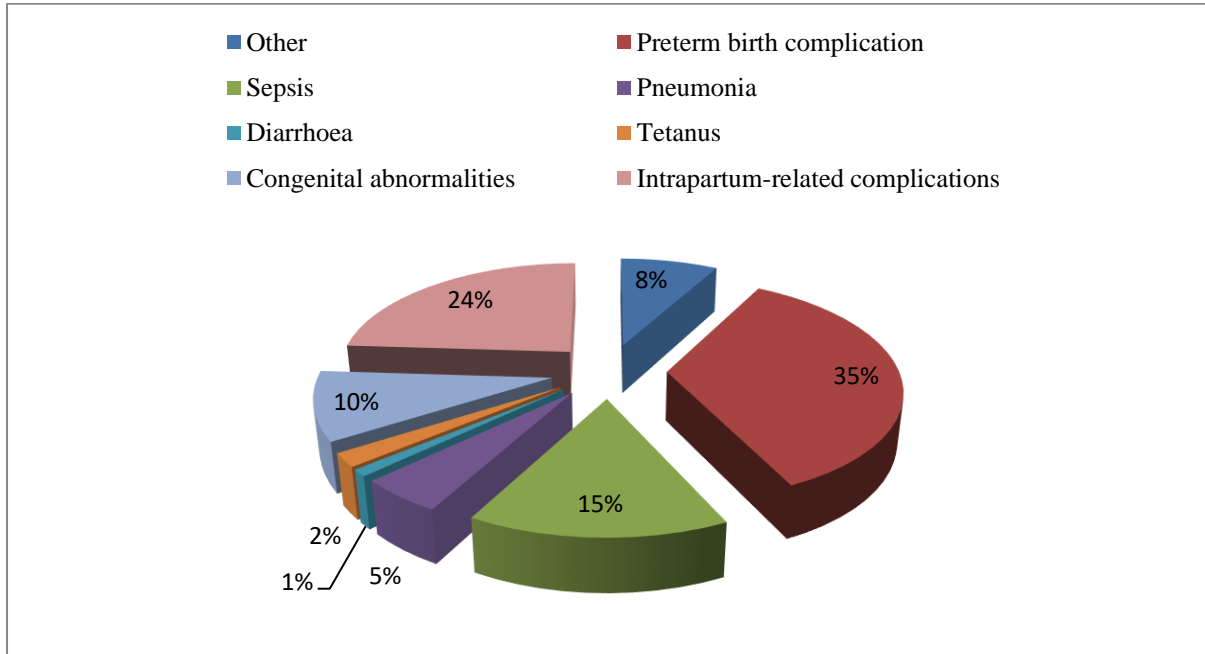


**Figure 1.** The pie chart explains statistical data for inflammation caused during the neonatal stage.

Presently, the microbial testing-based conventional method is used for sepsis detection. The presence of a pathogen is detected by providing similar growing conditions. The bacterial testing possesses specific limitations, such as producing false-negative results. The false-negative results are produced in cases where the maternal body is injected with antibodies. Besides, the method does not produce rapid results and takes 2-3 days for testing while making the delay causing worsen effects in serious cases. Therefore, the neonates are treated with antibiotics without the outcome of diagnostic results, and this may lead to the emergence of multiple drug-resistant bacteria in the ICU for neonates [10,11]. Thus, there is a need to develop an effective diagnostic test to avoid unnecessary empirical treatment [12].

Biomarkers can play a vital role in the early detection of sepsis by differentiating them from non-infectious disorders. Several biomarkers have been reported in the studies showing elevation in their level during inflammation, such as Tumor necrosis factor-alpha (TNF- $\alpha$ ), Fibronectin, Haptoglobin, Procalcitonin (PCT), Neopterin, Lipopolysaccharide binding (LPB), C-reactive protein (CRP), IFN- $\gamma$ -induced protein 10, Interleukin-1 $\beta$  (IL-1 $\beta$ ), Interleukine-8 (IL-8), CD11b, CD64 (Glycoprotein), sTREM-1, Serum amyloid A (SAA), and Interleukine-6 (IL-6) [13-15]. CRP is considered an acute-phase protein produced by the liver during inflammation in several medical conditions [16,17], which is limited to pathogenic infection. However, it was also reported in maternal fever or fetal distress. The low specificity of CRP is accepted. Therefore, a test in combination with CRP and other biomarkers such as SAA and PCT can better diagnose neonatal sepsis [18,19]. The range of CRP is classified into three categories based on the risk of sepsis for children. At a lower risk level, the concentration is  $\leq 10$  mg/L. Once the risk level is intermediate, the concentration is within a range of 11-100 mg/L, and at a higher risk level, the CRP concentration is  $>100$  mg/L [20]. The healthy adults

have a lower CRP level than 0.3 mg/dL, and in older people, it is found to be 0.2-3.0 mg/L [21].

Various studies have been reported for CRP detection through electrochemical sensing. A platform that was developed consisted of nano-hybrid material gold nanoparticles (Au NPs) and molybdenum disulfide (MoS<sub>2</sub>). The MoS<sub>2</sub> was functionalized with ionic liquid, and the primary anti-CRP was immobilized on the surface of it. Furthermore, graphene oxide (GO) was modified with 1,5-diaminonaphthalene (DN) for loading iridium nanoparticles (Ir NPs) to tag the secondary anti-CRP. The platform was evaluated with CRP antigen, and the results were recorded using the electrochemical technique [22]. Another study describes an electrochemical immunosensor designed for CRP detection based on the microelectrode array constituted in an interdigitated wave shape format. The electrode was modified using the dithiobis (succinimidyl propionate) (DTSP) monolayer self-assembled on the electrode surface. The anti-CRP was then immobilized on the surface for CRP determination [23]. In another reported work, a label-free electrochemical immunoassay was assembled for CRP determination. The sensor combines DNA-directed immobilization (DDI) on the microwire sensor, and the response was recorded with electrochemical impedance spectroscopy [24]. An electrochemical paper-based biosensor was developed on a screen-printed electrode (SPE) that was coated with gold nanoparticles. This presented biosensor was employed for the label-free determination of CRP. The SPE was further modified with self-assembly of poly(2-methacryloyloxyethyl phosphorylcholine) (PMPC-SH) where the thiol groups were terminated, and the reaction that occurred on the surface of the electrode was recorded with differential pulse voltammetry (DPV) [25].

Bimetallic nanoparticles are the combination of two different monometallic elements. They attract properties of both the metal and facilitate the unique properties (photocatalytic, electronic, and optical) generated through their combinations. These properties are not obtained with monometallic nanoparticles [26]. Gold nanoparticles have been considered an ideal material for biosensor development based on electrochemical detection techniques. The gold surface is beneficial in providing a microenvironment for binding between biomolecules. These nanoparticles (NPs) also act as a bridge between the working electrode and redox protein that enhances electron transfer on the electrode surface [27-31] and provides a high surface area [29]. Platinum nanoparticles (Pt NPs) are popularly used for biosensor development due to their various beneficial properties, such as conductivity, biocompatibility, and it also exhibits unique electrocatalytic activity towards H<sub>2</sub>O<sub>2</sub> [29,32]. Therefore, The surface of the Screen-printed carbon electrode (SPCE) was modified with bimetallic gold-platinum (Au-Pt) Nanomaterials (NMs) to provide the synergistic effect for enhancing the surface area and catalytic properties of the biosensor. The nanomaterials provide a higher surface-to-volume ratio and promote reducing the erosion or clogging on the surface of the electrode, thereby improving the thermodynamic properties of the developed system. In addition, the mass transport on the surface of molecularly imprinted polymer (MIP) modified electrode and binding affinity at the sites was enhanced [33-40].

Molecular imprinting is a self-assembled polymer matrix-based approach to create 3-Dimensional (3-D) imprinting structures for a specific target molecule [41-49]. The MIPs have various advantages over other sensing platforms based on proteins and nucleic acids. The important benefit of MIPs is they provide high selectivity and affinity for the template or target biomolecule. In addition, they are resistant at higher pressure and temperature, show higher strength, physical robustness, and inertness to organic solvents, bases, acids, and metal ions.

Moreover, low cost is required to synthesize MIPs, and their storage life is very long when stored carefully at room temperature [50]. Hence, the electrode was modified with MIPs prepared for CRP for the detection of neonatal sepsis. Further, the biosensor was evaluated with electrochemical techniques for voltammetric and impedimetric measurements. The fabricated biosensor operates in a wide detection range, with higher sensitivity and lower detection limit.

In this presented work, an electrochemical biosensor based on molecular imprinting was fabricated to identify a CRP biomarker. The biosensor development helps to overcome the limitations of traditional methods such as they are user-friendly, cost-effective, provide rapid response, can be developed into a point of care device, less sample volume is required, which is an especially important factor that is needed to be considered in the case of neonates.

## 2. Materials and Methods

### 2.1. Reagents and equipments.

C-reactive protein (purified from Human Serum, CAS no: CAS 9007-41-4) was obtained from Sigma Aldrich, U.S.A., Chloroauric acid ( $\text{HAuCl}_4 \cdot 4\text{H}_2\text{O}$ ), Chloroplatinic acid ( $\text{H}_2\text{PtCl}_6 \cdot 6\text{H}_2\text{O}$ ), Methyl methacrylate (MMA), Acetonitrile (ACN), Azobisisobutyronitrile (AIBN), Ethylene glycol dimethacrylate (EGDMA), Trisodium citrate was procured from Sisco Research Laboratories Pvt. Ltd., India. A screen-printed carbon electrode of dimension 8x10 (Working electrode (WE) with geometric area 7.07 mm<sup>2</sup>) was purchased from PalmSens Compact Electrochemical Interfaces. Distilled water (DW) was used for sample preparations.

Scanning electron microscopy (SEM) was performed to study the surface modification of the electrode. The elemental composition of the modified electrode was then determined with Energy-dispersive X-ray (EDX) spectroscopy. Besides, the surface morphology was examined with Atomic force microscopy (AFM), and X-ray diffraction (XRD) that were accomplished at Amity University, Noida, U.P. The pore size distribution of the imprinted polymer was studied by Brunauer-Emmett-Teller (BET). Electrochemical measurements were performed on Biologics potentiostat (specification: SP-150, EC-Lab software). This system combines 3 electrodes in an electrochemical cell consisting of an auxiliary, reference, and a working electrode. For completion of circuit and charge flow, all electrodes must be immersed into a mediator solution.

### 2.2. Synthesis of Au-Pt bimetallic nanocomposite.

The bimetallic Au-Pt nanomaterials were prepared in a 1:1 ratio. To prepare a 100 mL solution, 88 mL of DW was taken, and a 3.5 mL (0.01 M) mixture of  $\text{H}_2\text{PtCl}_6 \cdot 6\text{H}_2\text{O}$  and  $\text{HAuCl}_4 \cdot 4\text{H}_2\text{O}$  was dissolved. The prepared mixture was heated at 100 °C with steady stirring. A preheated solution of trisodium citrate (5 mL of 1 %) was immediately added to the boiling mixture. The color of the solution changes from yellowish to light purple. The solution was then allowed to boil for half an hour or until the color changed to dark purple [26,37,38].

### 2.3. Synthesis of molecularly imprinted polymer.

The MIP for C-reactive protein was synthesized using the bulk polymerization procedure. The synthesized process was carried with CRP (template), MMA (monomer), and EGDMA (crosslinker) in a specific ratio were added to 20 mL of ACN solution and was

sonicated for 45 min. and thereby treating the mixture with nitrogen (10 min.). While maintaining the inert conditions, the initiator (AIBN) was added to the solution at 35 °C and was further kept for polymerization in an oil bath for 48 hours; Scheme 1 shows the graphical illustration of steps involved in MIP synthesis. The white powder was obtained and washed with a solution of methanol and acetic acid in a ratio of 4:1 for 24 hours, and the final washing of the MIP was performed with methanol. The obtained product was then dried and crushed into fine powder [49].

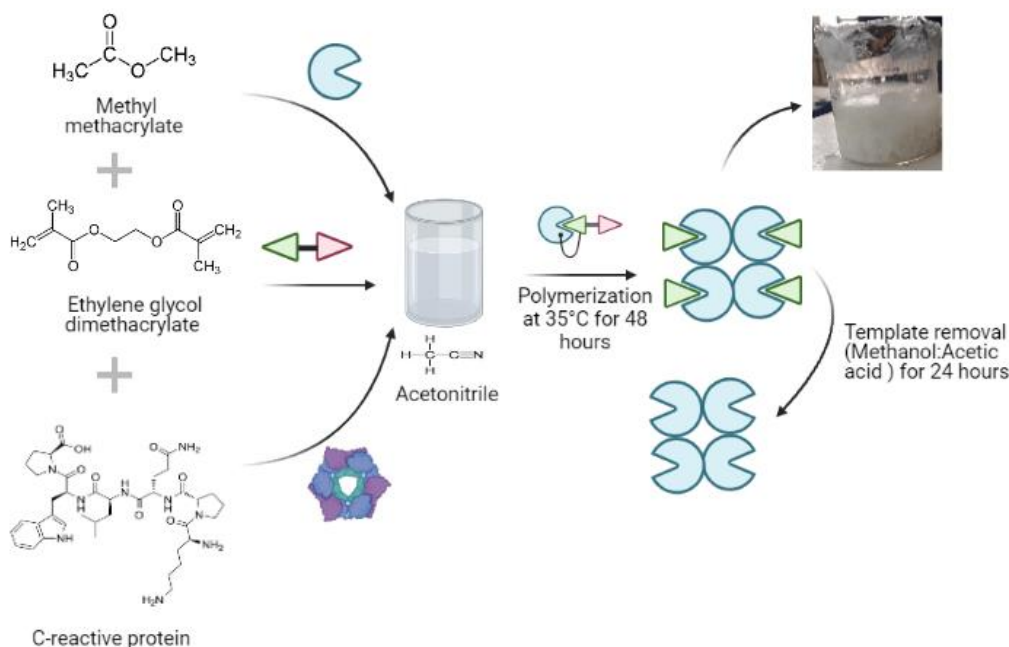


**Figure 1.** Schematic illustration for the synthesis of a molecularly imprinted polymer.

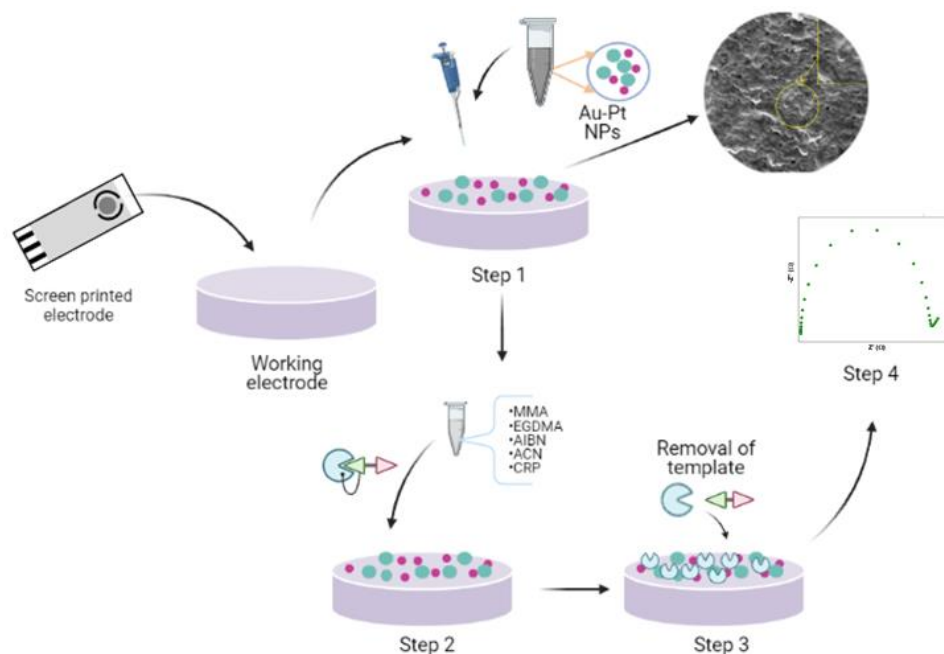


**Figure 2.** Graphical representation for the fabrication of working electrode: **Step-1:** Modifying the working electrode with Au-Pt NMs, electrodeposited on screen-printed carbon electrode using chronoamperometry at -0.2 V for 400 sec.; **Step-2:** Electrochemical deposition of MIP<sub>Tem</sub> on Au-Pt NMs/SPCE within a potential range from -0.2 V to +0.6 V for 15 cycles (scan rate at 20 mV/s); **Step-3:** Removal of template from the electrode surface with a solution of methanol and acetic acid (4:1); **Step-4:** Electrochemical measurements for developed biosensor.

#### 2.4. Fabrication of working SPCE

The working electrode was immersed in a mixture of mediator solution (ferro/ferri - 0.5 mM) containing  $\text{HAuCl}_4$  (1 mM) and  $\text{H}_2\text{PtCl}_6$  (1 mM). The electrodeposition was carried out by chronoamperometry at -0.2 V for 400 sec. The modified electrode was then washed with DW and dried at room temperature [26].

Further, the electrode was modified by electrodepositing MIP on the surface of Au-Pt NMs/SPCE modified electrode through Cyclic voltammetry (CV) within a potential range from -0.2 V to +0.6 V for 15 cycles (scan rate at 20 mV/s) [49]. Thereafter, the modified electrode was washed with DW, and kept for drying at room temperature for further experimentation. Scheme 2 illustrates the graphical model for steps involved in electrode fabrication.

### 3. Results and Discussion

#### 3.1. Surface morphology of the fabricated electrode.

The modified surface morphology was studied by Atomic force microscopy (AFM) with a 3-D model as shown in Figure 2 (a); the AFM analysis of the working electrode was observed within an  $8 \times 8 \mu\text{m}$  area. The elemental composition of synthesized NMs was determined by EDX; Figure 2 (b) confirms the presence of Au-Pt nanoparticles. SEM was included to study surface moderation of the electrode at each modification step. Figure 3 shows SEM micrographs of different modification stages for the electrode. In Figure 3 (a), the spherical structures confirm the modification of electrodes with the Au-Pt NMs. These bimetallic NMs enhance the surface area and catalytic properties of the biosensor. A structured pattern is visible in Figure 3 (b), confirming the deposition of  $\text{MIP}_{\text{Tem}}$ . The MIP shows improved selectivity and adsorption efficiency for the template. Further, the MIP was washed by removing the template (CRP) with methanol and acetic acid mixture. The cavities obtained after template removal are shown in Figure 3 (c). These cavities will be used for template binding with MIP in further experimentation. For control experiments, preparation of Non-imprinted polymer (NIP) was carried out by using appropriate quantities of monomer and crosslinker that is MMA and EGDMA, respectively, in ACN porogenic solution. The mixture was sonicated for 45 min. at room temperature and nitrogen, purging was carried out for 10 min. Further, the initiator AIBN was added to the mixture under inert conditions. The prepared solution was kept for polymerization at  $35^\circ\text{C}$  for 48 hours. After polymerization, the collected white product was dried and crushed into fine powder. Figure 3 (d) depicts the surface of NIP, indicating no defined pattern or structure on the electrode surface.

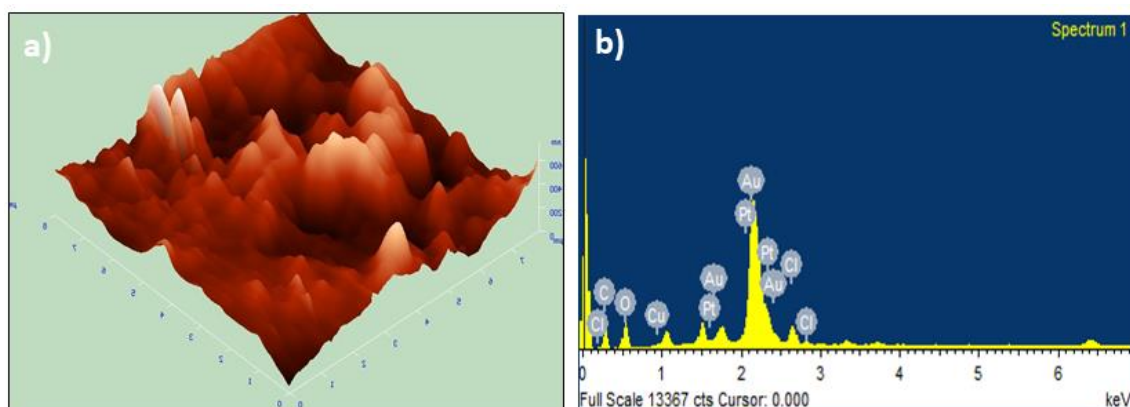


**Figure 2.** (a) Atomic force microscopy 3-D graph for Au-Pt modified electrode; (b) Energy-dispersive X-Ray analysis for prepared Au-Pt NMs.

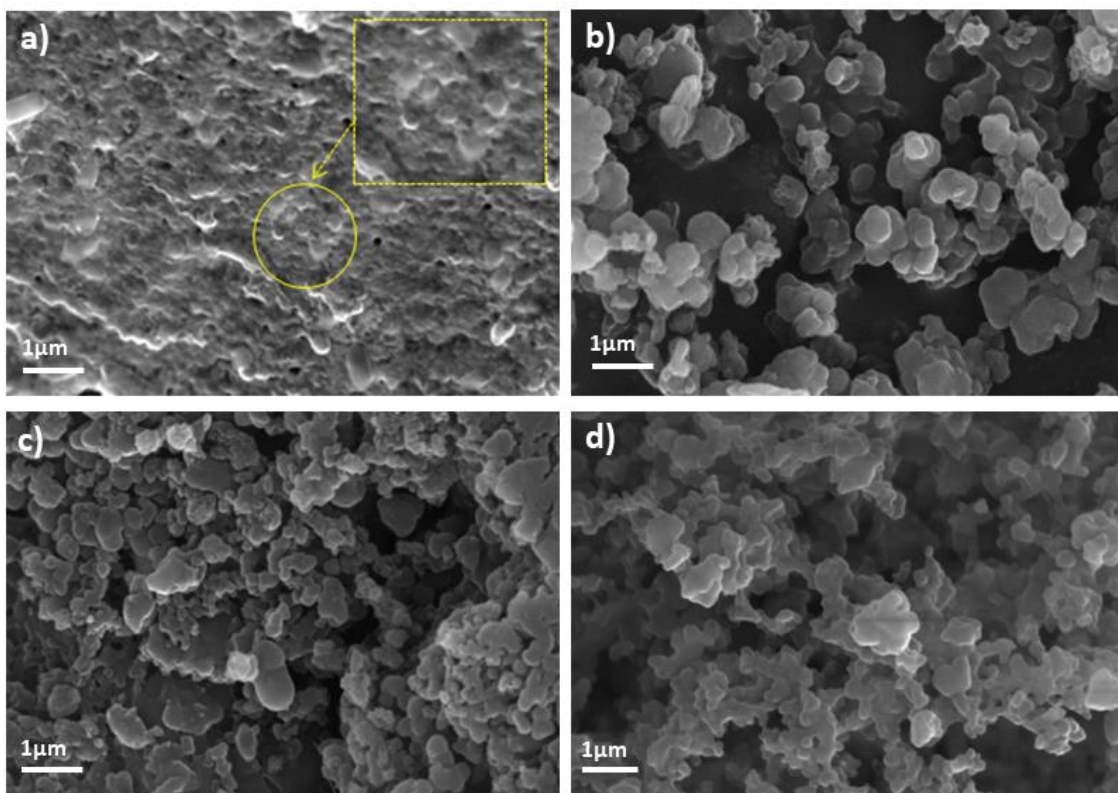


**Figure 3.** Scanning electron microscopy (a) Au-Pt NMs/SPCE, (b) MIP<sub>Tem</sub>/Au-Pt NMs/SPCE, (c) MIP/Au-Pt NMs/SPCE, and (d) Non-imprinted polymer.

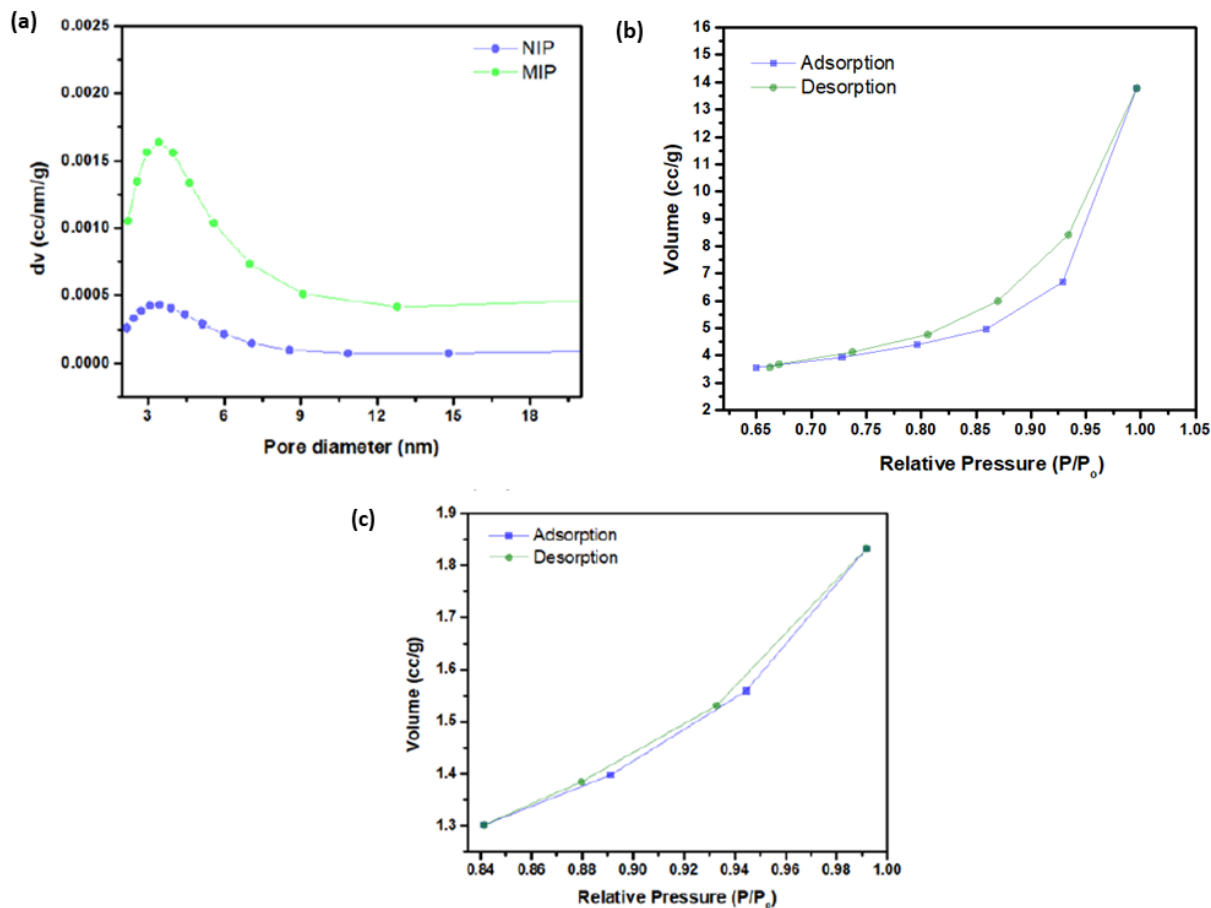


**Figure 4.** (a) Pore size distribution graph for MIP<sub>Tem</sub> and NIP; Adsorption and Desorption curve (b) MIP; (c) NIP.

The pore size of imprint after removing CRP (template) from imprinted polymer was characterized by BET. Figure 4 shows the BET analysis graph for MIP. Figure 4 (a) describes the curve for the pore size distribution of MIP and NIP as control. The pore size obtained for MIP was 9.358 m<sup>2</sup>/g and 7.146 m<sup>2</sup>/g for NIP (Table 1). Figure 4 (b) and (c) depicts the type-1 adsorption and desorption isotherm graph for MIP and NIP as control, respectively explaining monolayer adsorption for the adsorbent. Due to the distortion of monolayer adsorption, no further adsorption was observed in the sample since the molecules were clumped with each other. Figure 5 describes XRD an analysis that was performed for MIP<sub>Tem</sub>, MIP, and NIP samples. The graph shows no specific peaks within a spectrum, confirming that the synthesized material is amorphous.

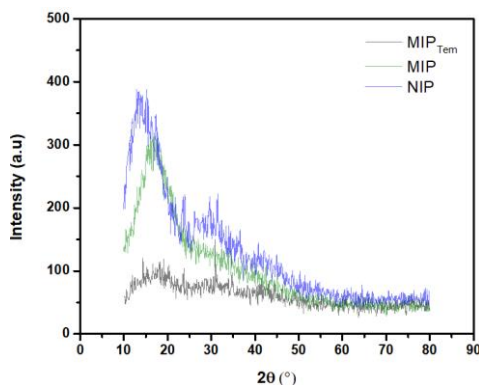


**Figure 5.** X-ray diffraction graph for MIP<sub>Tem</sub>; MIP and NIP.

**Table 1.** BET analysis for synthesized MIP and NIP.

Polymer	Surface area (m <sup>2</sup> /g)	Pore volume (cm <sup>3</sup> /g)	Pore diameter (nm)
MIP	9.358	0.032	2.56
NIP	7.146	0.003	2.183

### 3.2. Performance and Evaluation of MIP/Au-Pt NMs/SPCE electrode by electrochemical techniques.

#### 3.2.1. Cyclic voltammetry studies for the fabricated electrode.

The stepwise modification of the electrode was studied by a CV, as shown in Figure 6. The CV was performed between the potential ranging from -0.5 V to +0.5 V in a ferro/ferri (0.5 mM) mediator solution. The lowest oxidation and reduction peaks were observed with the bare electrode in mediator solution as +0.012 mA and -0.011 mA, respectively. Once the electrode was modified with Au-Pt NMs, the maximum oxidation and reduction peaks were obtained due to the synergistic effect of NMs on the surface of the fabricated electrode caused by increasing the electron transfer rate. Further, MIP<sub>Tem</sub> was electrodeposited on an electrode surface, showing a decline in oxidation peak. Then, MIP was washed for template removal, and a CV graph was obtained; the MIP showed an increase in the oxidation and reduction current. The peak current may be increased due to the specific capability of MIP for recognizing the template (CRP). The diffusion of CRP molecules occurs on the electrode surface through the cavities created because of template removal and undergoes a redox reaction. Further, a control experiment was performed with PBS to study the electrode behavior. It was observed that the peak current is declined in the presence of PBS.

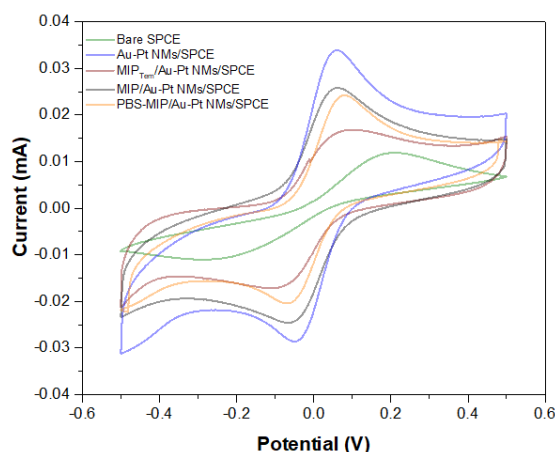


**Figure 6.** Electrode modification. Cyclic voltammety of Bare SPCE, Au-Pt NMs/SPCE, MIP<sub>Tem</sub>/Au-Pt NMs/SPCE, MIP/Au-Pt NMs/SPCE, and PBS-MIP/Au-Pt NMs/SPCE, in ferro/ferri mediator solution of 0.5 mM within potential range -0.5 V to +0.5 V at scan rate 20 mV/s.

### 3.2.2. Electrochemical impedance study for MIP/Au-Pt NMs/SPCE modified electrode.

The resistance charge transfer property of the modified electrode was measured with Electrochemical impedance spectroscopy (EIS). As described in Figure 7, the Nyquist plot shows the semi-circle depicting the Resistance charge transfer (R<sub>ct</sub>) and the linear part showing the diffusion process.

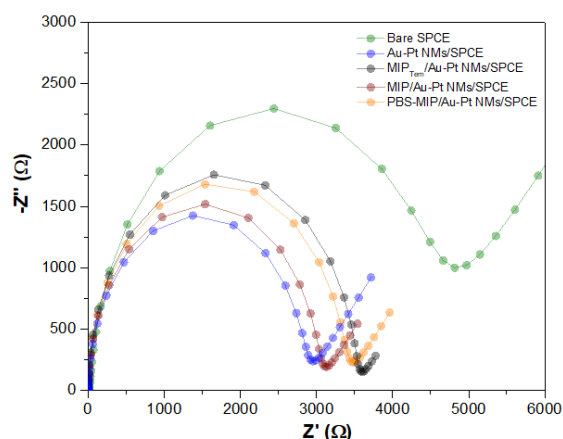


**Figure 7.** Electrode modification study with electrochemical impedance spectroscopy of Bare SPCE, Au-Pt NMs/SPCE, MIP<sub>Tem</sub>/Au-Pt NMs/SPCE, MIP/Au-Pt NMs/SPCE, and PBS-MIP/Au-Pt NMs/SPCE in ferro/ferri mediator solution of 0.5 mM at frequencies: F<sub>initial</sub>-100 Khz and F<sub>final</sub>-100 mhz.

A higher R<sub>ct</sub> value was obtained with a bare electrode in mediator solution due to increased internal resistance of the system. Further, the R<sub>ct</sub> value was decreased with modification of the electrode, and the lowest R<sub>ct</sub> value was obtained with Au-Pt NMs. The results obtained were similar to CV observations, supporting maximum conductivity.

### 3.3. Optimization studies for the MIP/Au-Pt NMs/SPCE biosensor.

#### 3.3.1. Catalytic performance of the modified electrode (MIP/Au-Pt NMs/SPCE).

The electrode was evaluated with distinct CRP concentrations ranging within 0.1 nM to 500 nM (0.1 nM, 0.5 nM, 1 nM, 10 nM, 100 nM, 200 nM, 500 nM) by EIS in a ferro/ferri mediator solution of 0.5 mM. Figure 8 (a) depicts the Nyquist plot for varying CRP concentrations on an electrode surface. The curve shows that while decreasing the CRP

concentrations, Rct value of the system decreases from 4.62 to 2.31 KΩ. Thus, low resistance and higher electron charge are generated at lower concentrations. This clearly describes that an increasing concentration blocks the binding of CRP to imprinted polymer on the electrode surface. As shown in Figure 8 (b), a calibration graph was plotted by evaluating the Rct value and varying concentrations. Similarly, the sensor's Square wave voltammetry (SWV) response was plotted as shown in Figure 8 (c). Further, considering the peak current value and log concentrations, a calibration graph was drawn, as shown in Figure 8 (d). The graphs show a gradual reduction of peak current with the proportional increase in CRP concentration. The sensitivity of the fabricated biosensor was calculated as 0.14 μA/nM (with SWV response), and the detection limit of the biosensor was observed as 0.1 nM. The obtained results for the developed sensing platform are summarized in Table 2.

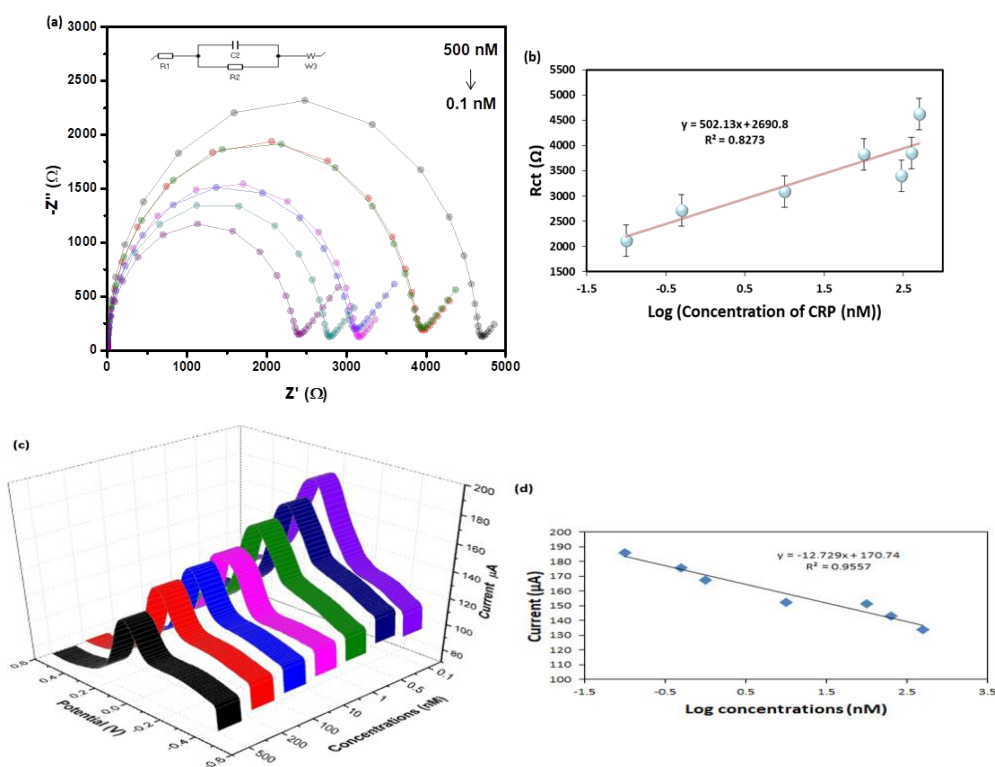


**Figure 8.** Concentration studies: (a) Impedance study for different CRP concentrations on modified MIP/Au-Pt NMs/SPCE electrode (0.1 nM, 0.5 nM, 1 nM, 10 nM, 100 nM, 200 nM, and 500 nM) in ferro/ferri mediator solution of 0.5 mM at frequencies:  $F_{initial}$ -100 KHz and  $F_{final}$ -100 mhz; (b) Calibration graph with log concentrations versus Rct value obtained with different concentrations; (c) Square wave voltammetry with varying concentrations; (d) Standard calibration graph with peak current.

**Table 2.** Summary of the distinct parameters observed in the present study for CRP detection.

S.No.	Parameter	Value
1.	Sensitivity	0.14 μA/nM
2.	Detection limit	0.1 nM
3.	Linear range	0.1 nM - 500 nM
4.	Sample volume	<5 μL
5.	Regression coefficient	0.95
6.	Response time	< 5 min

### 3.3.2. Scan rate effect on the developed biosensor.

The kinetic effect of the reaction on the electrode surface was studied with variable scan rates. The study was carried out with varying scan rate values from 20 to 140 mV/s in a ferro/ferri (0.5 mM) mediator solution using CV, as shown in Figure 9 (a). The graph shows

an increase in anodic and cathodic peaks with a simultaneous increase in scan rate within a constant potential range from -0.4 V to +0.4 V. Figure 9 (b) shows a calibration graph plotted for square root value of scan rate ( $\sqrt{v}$ ) versus peak current for both anodic and cathodic peak.

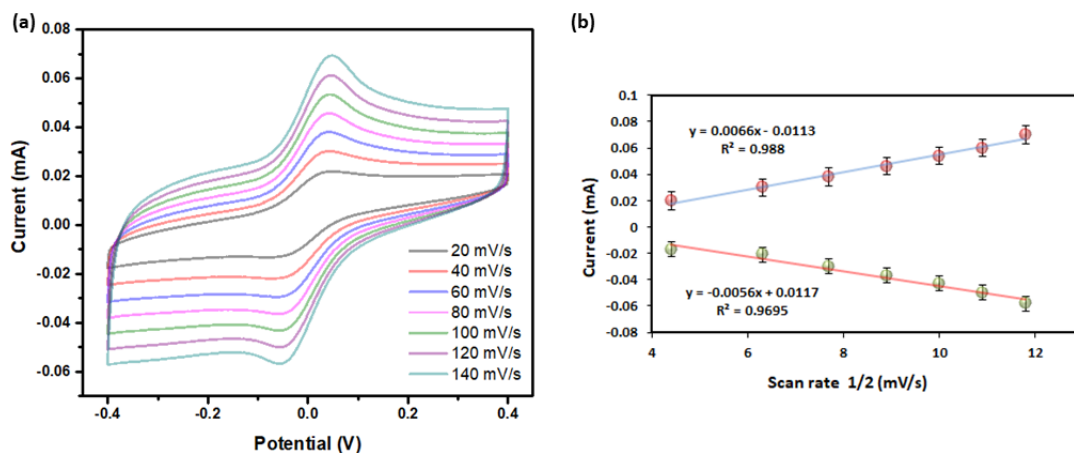


**Figure 9.** Optimizing fabricated biosensor: (a) Scan rate studies for fabricated MIP/Au-Pt NMs/SPCE electrode with 0.1 nM CRP concentration in ferro/ferri mediator solution of 0.5 mM within a potential range from -0.4 V to +0.4 V at different scan rates 20 to 140 mV/s; (b) Calibration graph for peak current vs. square root of scan rate.

### 3.3.3. pH studies for the biosensor.

The fabricated MIP/Au-Pt NMs/SPCE electrode was optimized with varying pH ranging from pH 5.5 to 8.5. The study was carried out using SWV with constant CRP concentration (0.1 nM) in a ferro/ferri mediator solution (0.5 mM). A bar graph was plotted for peak current versus varying pH values, as shown in Figure 10. The peak current was increased from pH 5.5 to 6.5 and gradually decreased afterward. The initial increment of an anodic peak can be justified by the hydrogen bond formation between  $-NH_2$  group of MMA and the H-H group of CRP. Whereas deprotonation occurred with a further increase in the pH; hence, hydrogen bonding between the groups weakened, and the current peak is decreased [51].

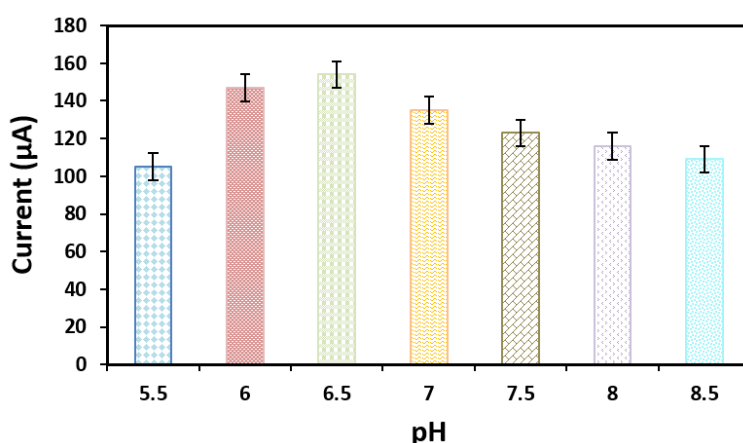


**Figure 10.** Effect of pH on the MIP/Au-Pt NMs/SPCE modified electrode with different pH values 5.5, 6.0, 6.5, 7.0, 7.5, 8.0 and 8.5 pH at -0.5 V.

### 3.3.4. Temperature optimization for the MIP/Au-Pt NMs/SPCE biosensor

In order to identify the optimum temperature for the biosensor, the performance of the electrode was evaluated at distinct temperatures ranging from 10 to 70 °C with an interval of

10 °C. Figure 11 shows the bar graph of evaluated temperatures for modified electrodes dipped in a ferro/ferri mediator solution (0.5 mM). The current response was gradually increased for temperature from 10 to 30 °C and thereby decreased. Therefore 30 °C was selected as an optimum temperature for further experimentations. Further, the response time for the electrode was observed as less than 5 min.

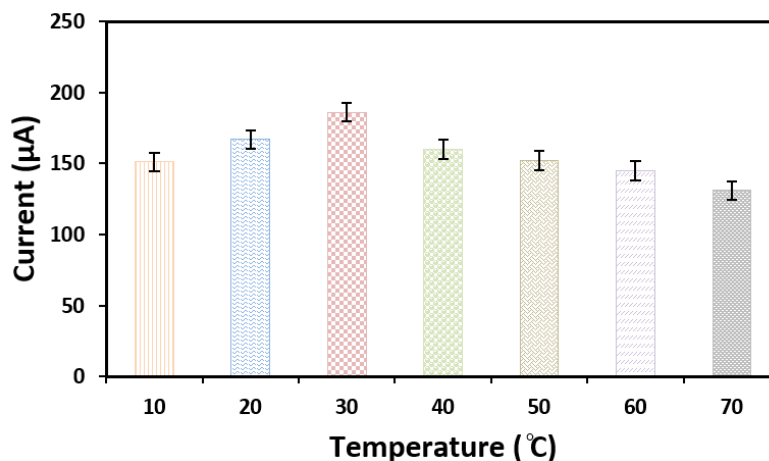


**Figure 11.** Result of temperature variation on the MIP/Au-Pt NMs/SPCE modified electrode within a range from 10 to 70°C with an interval of 10°C at -0.5 V.

### 3.4. Interference studies.

Interference study for the developed electrode was carried out with glucose (C<sub>6</sub>H<sub>12</sub>O<sub>6</sub>), uric acid (C<sub>5</sub>H<sub>4</sub>N<sub>4</sub>O<sub>3</sub>), acetylcholine (Ach), cholesterol (C<sub>27</sub>H<sub>46</sub>O), ascorbic acid (C<sub>6</sub>H<sub>8</sub>O<sub>6</sub>), SAA, TNF-α, PCT at a concentration of 0.1 nM. Figure 12 shows the graph for the activity of the developed biosensor (%) with different compounds. The variation in the current (loss in biosensor activity) with other antigens was below 15% when comparing it with the response obtained with CRP. The results show that the biosensor retains higher selectivity.

Electrochemical characteristics of biosensors are outlined in Table 3, indicating a comparison of previously reported sensors with present work. The proposed biosensor exhibits a wide detection range and low detection time. The sensor possesses excellent properties such as high sensitivity and specificity, rapid result production, small size, and no proficient professional is required for operation. Hence it can be developed into a portable device.

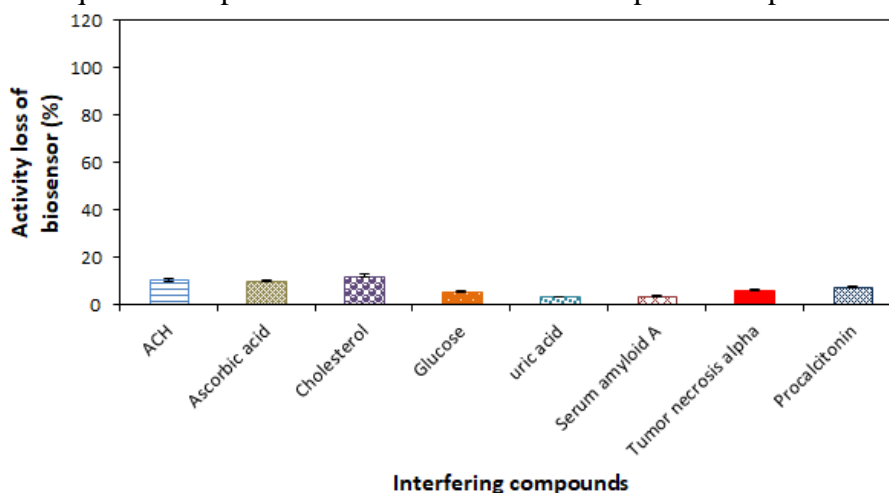


**Figure 12.** Interference study on developed MIP/Au-Pt NMs/SPCE modified electrode with different compounds (glucose, uric acid, ascorbic acid, acetylcholine, cholesterol, SAA, TNF-α, and PCT) in ferro/ferri mediator solution of 0.5 mM.

**Table 3.** Comparison of electrochemical parameters of reported and developed biosensors for CRP detection.

S.No.	Platform/electrode substrate	Limit of detection	Detection range	Response time	References
1.	Polycrystalline gold electrode	176 pM	0.5-50 nM	10-15 min.	[17]
2.	GQD-based CRP biosensor	176 pM	0.5-70 nM	NR	[52]
3.	Poly(EDOT-co-EDOTPC)	37 nM	10-160 nM	NR	[53]
4.	SAM/Au NPs/SPCE	0.15 nM	0.4-200 nM	30 min.	[54]
5.	MIP/Au-Pt NMs/SPCE	0.1 nM	0.1 nM-500 nM	< 5 min.	Present work

GQD: Graphene quantum dots; CRP: C-reactive protein; EDOT: 3,4-Ethylenedioxythiophene; SAM: Self-assembled monolayer; Au NPs: Gold nanoparticles; MIP: Molecularly imprinted polymer; NMs: Nanomaterials; Au-Pt: Gold-platinum; SPCE: Screen-printed carbon electrode; NR-Not reported

### 3.5. Stability and repeatability of the developed biosensor

The stability of the electrode was checked while storing it in a dry condition at 4 °C. The electrode was continuously monitored every seventh day up to 3 months (Figure S1 of supplementary file). The activity of the electrode was reduced up to 70% after 6 weeks. To check the reproducibility of the fabricated biosensor, five identical electrodes were prepared under similar conditions (Figure 13). The obtained results showed a minimal current difference for each electrode. The RSD (%) value of 0.09% was calculated for the average current obtained with similar electrodes.

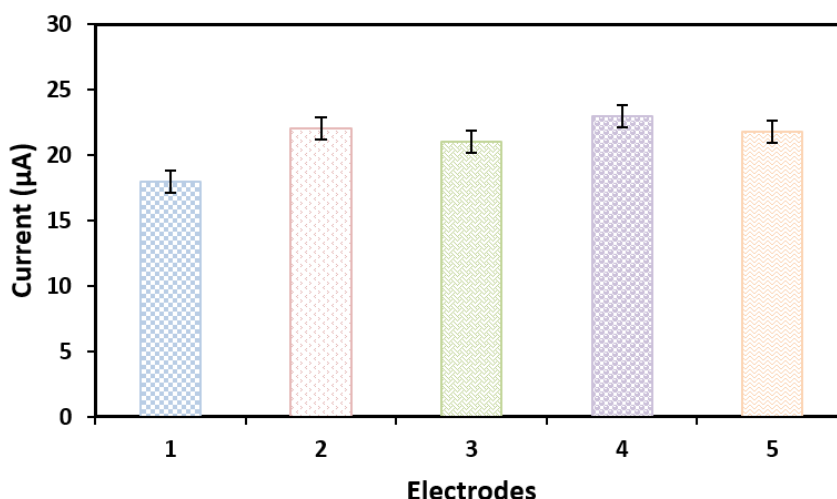


**Figure 13.** The reproducibility for MIP/Au-Pt NMs/SPCE modified electrode was observed with five identically prepared electrodes.

## 4. Conclusions

Recently, the studies recommended the CRP biomarker can benefit the precocious detection of neonatal sepsis. It is a prognostic marker and is widely used in diagnosis. It has already been reported that CRP level may include accompaniment in risk factors and clinical signs during neonatal sepsis detection. In the previous reports, CRP has been considered an important biomarker for diagnosing neonatal sepsis in the early stages. It starts rising within 4 to 6 hours after inflammation, and the peak value can be obtained between 24 and 48 hours of onset. It has high sensitivity and specificity as compared with other neonatal sepsis biomarkers. Hence, in this presented work, CRP was considered to develop the sensing platform that can be used for neonatal sepsis detection.

A biosensing platform for the detection of C-reactive protein was fabricated on SPCE. The electrode was coated with bimetallic nanomaterials (Au-Pt) to increase its conductivity.

Furthermore, the electrode was improved with electrodeposition of MIP prepared for CRP. The coating of MIP on sensing platforms triggers higher selectivity and sensitivity. The template was removed from MIP, on the electrode surface to obtain cavities for the CRP molecule, and its electrochemical response was observed. The fabricated biosensor exhibits a lower detection limit of 0.1 nM and a wide detection range from 0.1 nM to 500 nM. The sensitivity of the sensor was calculated as 0.14  $\mu\text{A/nM}$ . The sensing platform provides fast response, operates in a broad concentration range, and exhibits a lower detection limit, so this can be advanced into a point of care device.

## Funding

No external financial funding support was received for this research work.

## Acknowledgments

Not applicable.

## Conflicts of Interest

All the authors presenting this manuscript declare there is no financial or personal conflict of interest.

## References

1. Jia, Y.; Wang, Y.; Yu, X. Relationship between blood lactic acid, blood procalcitonin, C-reactive protein and neonatal sepsis and corresponding prognostic significance in sick children. *Experimental and therapeutic medicine*. **2017**, *14*, 2189-2193, <https://doi.org/10.3892/etm.2017.4713>.
2. Odabasi, I.O.; Bulbul, A. Neonatal sepsis. *The Medical Bulletin of Sisli Etfal Hospital*. **2020**, *54*, 142-158, <https://doi.org/10.14744/SEMB.2020.00236>.
3. Stoll, B.J.; Hansen, N.I.; Adams-Chapman, I.; Fanaroff, A.A.; Hintz, S.R.; Vohr, B.; Higgins, R.D. Neurodevelopmental and growth impairment among extremely low-birth-weight infants with neonatal infection. *Jama*. **2004**, *292*, 2357-2365, <https://doi.org/10.1001/jama.292.19.2357>.
4. Vergnano, S.; Sharland, M.; Kazembe, P.; Mwansambo, C.; Heath, P.T. Neonatal sepsis: an international perspective. *Archives of Disease in Childhood-Fetal and Neonatal Edition*. **2005**, *90*, F220-F224, <http://dx.doi.org/10.1136/adc.2002.022863>.
5. Oeser, C.; Pond, M.; Butcher, P.; Bedford Russell, A.; Henneke, P.; Laing, K.; Planche, T.; Heath, P.T.; Harris, K. PCR for the detection of pathogens in neonatal early onset sepsis. *PLoS One*. **2020**, *15*, e0226817, <https://doi.org/10.1371/journal.pone.0226817>.
6. Manouni, E.L.; Hassani, S.; Niemarkt, H.J.; Berkhout, D.J.; Peeters, C.F.; Hulzebos, C.V.; van Kaam, A.H.; Kramer, B.W.; van Lingen, R.A.; Jenken, F.; de Boode, W.P.; Benninga, M.A. Profound Pathogen-Specific Alterations in Intestinal Microbiota Composition Precede Late-Onset Sepsis in Preterm Infants: A Longitudinal, Multicenter, Case-Control Study. *Clinical Infectious Diseases*. **2021**, *73*, , 224-232, <https://doi.org/10.1093/cid/ciaa1635>.
7. Stoll, B.J.; Hansen, N.I.; Higgins, R.D.; Fanaroff, A.A.; Duara, S.; Goldberg, R.; Lupton, A.; Walsh, M.; Oh, W.; Hale, E. Very low birth weight preterm infants with early onset neonatal sepsis: the predominance of gram-negative infections continues in the National Institute of Child Health and Human Development Neonatal Research Network, 2002–2003. *The Pediatric infectious disease journal*. **2005**, *24*, 635-639, <https://doi.org/10.1097/01.inf.0000168749.82105.64>.
8. Stoll, B.J.; Hansen, N.; Fanaroff, A.A.; Wright, L.L.; Carlo, W.A.; Ehrenkranz, R.A.; Lemons, J.A.; Donovan, E.F.; Stark, A.R.; Tyson, J.E.; Oh, W. Late-onset sepsis in very low birth weight neonates: the experience of the NICHD Neonatal Research Network. *Pediatrics*. **2002**, *110*, 285-291, <https://doi.org/10.1542/peds.110.2.285>.

9. Tang, X.J.; Sun, B.; Ding, X.; Li, H.; Feng, X. Changing trends in the bacteriological profiles and antibiotic susceptibility in neonatal sepsis at a tertiary children's hospital of China. *Translational Pediatrics*. **2020**, *9*, 734-742, <https://doi.org/10.21037/tp-20-115>.
10. Baraff, L.J. Clinical policy for children younger than three years presenting to the emergency department with fever. *Annals of emergency medicine*. **2003**, *42*, 546-549, [https://doi.org/10.1067/s0196-0644\(03\)00628-0](https://doi.org/10.1067/s0196-0644(03)00628-0).
11. Bouadma, L.; Luyt, C.E.; Tubach, F.; Cracco, C.; Alvarez, A.; Schwebel, C.; Schortgen, F.; Lasocki, S.; Veber, B.; Dehoux, M.; Bernard, M. Use of procalcitonin to reduce patients' exposure to antibiotics in intensive care units (PRORATA trial): a multicentre randomised controlled trial. *The Lancet*. **2010**, *375*, 463-474, [https://doi.org/10.1016/S0140-6736\(09\)61879-1](https://doi.org/10.1016/S0140-6736(09)61879-1).
12. Abdollahi, A.; Shoar, S.; Nayyeri, F.; Shariat, M. Diagnostic value of simultaneous measurement of procalcitonin, interleukin-6 and hs-CRP in prediction of early-onset neonatal sepsis. *Mediterranean journal of hematology and infectious diseases*. **2012**, *4*, e2012028, <https://doi.org/10.4084/MJHID.2012.028>.
13. Sakyi, S.A.; Enimil, A.; Adu, D.K.; Ephraim, R.D.; Danquah, K.O.; Fondjo, L.; Baidoe-Ansah, D.; Adoba, P.; Toboh, E.; Afranie, B.O. Individual and combined bioscore model of presepsin, procalcitonin, and high sensitive C-reactive protein as biomarkers for early diagnosis of paediatric sepsis. *Heliyon*. **2020**, *6*, e04841, <https://doi.org/10.1016/j.heliyon.2020.e04841>.
14. Chauhan, N.; Tiwari, S.; Jain, U. Potential biomarkers for effective screening of neonatal sepsis infections: An overview. *Microbial pathogenesis*. **2017**, *107*, 234-242, <https://doi.org/10.1016/j.micpath.2017.03.042>.
15. Balayan, S.; Chauhan, N.; Chandra, R.; Kuchhal, N.K.; Jain, U. Recent advances in developing biosensing based platforms for neonatal sepsis. *Biosensors and Bioelectronics*. **2020**, *25*, 112552, <https://doi.org/10.1016/j.bios.2020.112552>.
16. Kim, J.; Park, J.A.; Yim, G.; Jang, H.; Kim, T.H.; Sohn, H.; Lee, T. Fabrication of an electrochemical biosensor composed of multi-functional Ag ion intercalated DNA four-way junctions/rhodium nanoplate heterolayer on a micro-gap for C-reactive protein detection in human serum. *Analyst*. **2021**, *146*, 2131-2137, <https://doi.org/10.1039/D0AN02135K>.
17. Bryan, T., Luo, X., Bueno, P.R.; Davis, J.J. An optimised electrochemical biosensor for the label-free detection of C-reactive protein in blood. *Biosensors and Bioelectronics*. **2013**, *39*, 94-98, <https://doi.org/10.1016/j.bios.2012.06.051>.
18. Cetinkaya, M.; Özkan, H.; Köksal, N.; Celebi, S.; Hacimustafaoğlu, M. Comparison of serum amyloid A concentrations with those of C-reactive protein and procalcitonin in diagnosis and follow-up of neonatal sepsis in premature infants. *Journal of Perinatology*. **2009**, *29*, 225-231, <https://doi.org/10.1038/jp.2008.207>.
19. MR Umran, R., M Hashim, J., Jameel, H. Significance of Serum Procalcitonin Level in the Early Diagnosis of Neonatal Sepsis. *Iranian Journal of Neonatology IJN*. **2020**, *11*, 1-6, <https://doi.org/10.22038/IJN.2020.42296.1702>.
20. Lai, M.Y.; Tsai, M.H.; Lee, C.W.; Chiang, M.C.; Lien, R.; Fu, R.H.; Huang, H.R.; Chu, S.M. and Hsu, J.F. Characteristics of neonates with culture-proven bloodstream infection who have low levels of C-reactive protein ( $\leq 10$  mg/L). *BMC infectious diseases*. **2015**, *15*, 1-9, <https://doi.org/10.1186/s12879-015-1069-7>.
21. Wyczalkowska-Tomasik, A.; Czarkowska-Paczek, B.; Zielenkiewicz, M. and Paczek, L. Inflammatory markers change with age, but do not fall beyond reported normal ranges. *Archivum immunologiae et therapiae experimentalis*. **2016**, *64*, 249-254, <https://doi.org/10.1007/s00005-015-0357-7>.
22. Ma, Y.; Yang, J.; Yang, T.; Deng, Y.; Gu, M.; Wang, M.; Hu, R. and Yang, Y. Electrochemical detection of C-reactive protein using functionalized iridium nanoparticles/graphene oxide as a tag. *RSC Advances*. **2020**, *10*, 9723-9729, <https://doi.org/10.1039/C9RA10386D>.
23. Chinnadayala, S.R.; Park, J.; Kim, Y.H.; Choi, S.H.; Lee, S.M.; Cho, W.W.; Lee, G.Y.; Pyun, J.C. and Cho, S. Electrochemical detection of C-reactive protein in human serum based on self-assembled monolayer-modified interdigitated wave-shaped electrode. *Sensors*. **2019**, *19*, 5560, <https://doi.org/10.3390/s19245560>.
24. Songjaroen, T.; Feeny, R.M.; Mensack, M.M.; Laiwattanapaisal, W.; Henry, C.S. Label-free detection of C-reactive protein using an electrochemical DNA immunoassay. *Sensing and bio-sensing research*. **2016**, *8*, 14-19. <https://doi.org/10.1016/j.sbsr.2016.03.003>.
25. Pinyorosphatum, C.; Chaiyo, S.; Sae-Ung, P.; Hoven, V.P.; Damsongsang, P.; Siangproh, W.; Chailapakul, O. Disposable paper-based electrochemical sensor using thiol-terminated poly (2-methacryloyloxyethyl phosphorylcholine) for the label-free detection of C-reactive protein. *Microchimica Acta*. **2019**, *186*, 1-10, <https://doi.org/10.1007/s00604-019-3559-6>.

26. Jain, U.; Gupta, S.; Chauhan, N. Construction of an amperometric glycated hemoglobin biosensor based on Au–Pt bimetallic nanoparticles and poly (indole-5-carboxylic acid) modified Au electrode. *International journal of biological macromolecules*. **2017**, *105*, 549-555, <https://doi.org/10.1016/j.ijbiomac.2017.07.084>.
27. Chauhan, N.; Singh, A.; Narang, J.; Dahiya, S.; Pundir, C.S. Development of amperometric lysine biosensors based on Au nanoparticles/multiwalled carbon nanotubes/polymers modified Au electrodes. *Analyst*. **2012**, *137*, 5113-5122, <https://doi.org/10.1039/C2AN35629E>.
28. Chauhan, N.; Narang, J.; Pundir, C.S. Immobilization of rat brain acetylcholinesterase on porous gold-nanoparticle–CaCO<sub>3</sub> hybrid material modified Au electrode for detection of organophosphorous insecticides. *International journal of biological macromolecules*, **2011**, *49*, 923-929, <https://doi.org/10.1016/j.ijbiomac.2011.08.006>.
29. Chauhan, N.; Narang, J.; Pundir, C.S. Immobilization of lysine oxidase on a gold–platinum nanoparticles modified Au electrode for detection of lysine. *Enzyme and microbial technology*. **2013**, *52*, 265-271, <https://doi.org/10.1016/j.enzmictec.2013.01.006>.
30. Chauhan, N.; Narang, J.; Pundir, C.S. Immobilization of barley oxalate oxidase onto gold–nanoparticle-porous CaCO<sub>3</sub> microsphere hybrid for amperometric determination of oxalate in biological materials. *Clinical biochemistry*. **2012**, *45*, 253-258, <https://doi.org/10.1016/j.clinbiochem.2011.12.004>.
31. Jain, U.; Singh, A.; Kuchhal, N.K.; Chauhan, N. Glycated hemoglobin biosensing integration formed on Au nanoparticle-dotted tubular TiO<sub>2</sub> nanoarray. *Analytica chimica acta*. **2016**, *945*, 67-74, <https://doi.org/10.1016/j.aca.2016.09.026>.
32. Gupta, S.; Tiwari, A.; Jain, U.; Chauhan, N. Synergistic effect of 2D material coated Pt nanoparticles with PEDOT polymer on electrode surface interface for a sensitive label free *Helicobacter pylori* CagA (Ag-Ab) immunosensing. *Materials Science and Engineering: C*. **2019**, *103*, 109733, <https://doi.org/10.1016/j.msec.2019.05.018>.
33. Liu, F.F.; Zhao, X.P.; Kang, B.; Xia, X.H.; Wang, C. Non-linear mass transport in confined nanofluidic devices for label-free bioanalysis/sensors. *TrAC Trends in Analytical Chemistry*. **2020**, *123*, 115760, <https://doi.org/10.1016/j.trac.2019.115760>.
34. Asadikia, A.; Mirjalily, S.A.; Nasirizadeh, N.; Kargarsharifabad, H. Characterization of thermal and electrical properties of hybrid nanofluids prepared with multi-walled carbon nanotubes and Fe<sub>2</sub>O<sub>3</sub> nanoparticles. *International Communications in Heat and Mass Transfer*. **2020**, *117*, 104603. <https://doi.org/10.1016/j.icheatmasstransfer.2020.104603>.
35. Soltani, O.; Akbari, M. Effects of temperature and particles concentration on the dynamic viscosity of MgO-MWCNT/ethylene glycol hybrid nanofluid: experimental study. *Physica E: Low-dimensional Systems and Nanostructures*. **2016**, *84*, 564-570, <https://doi.org/10.1016/j.physe.2016.06.015>.
36. Arshad, W.; Ali, H.M. Experimental investigation of heat transfer and pressure drop in a straight minichannel heat sink using TiO<sub>2</sub> nanofluid. *International Journal of Heat and Mass Transfer*. **2017**, *110*, 248-256, <https://doi.org/10.1016/j.ijheatmasstransfer.2017.03.032>.
37. Essinger-Hileman, E.R.; DeCicco, D.; Bondi, J.F.; Schaak, R.E. Aqueous room-temperature synthesis of Au–Rh, Au–Pt, Pt–Rh, and Pd–Rh alloy nanoparticles: fully tunable compositions within the miscibility gaps. *Journal of Materials Chemistry*. **2011**, *21*, 11599-11604, <https://doi.org/10.1039/C0JM03913F>.
38. Jawad, M.; Ali, S.; Waseem, A.; Rabbani, F.; Amin, B.A.; Bilal, M.; Shaikh, A.J. Plasmonic effects and size relation of gold-platinum alloy nanoparticles. *Advances in nano research*. **2019**, *7*, 169-180, <http://dx.doi.org/10.12989/anr.2019.7.3.169>.
39. Chauhan, N.; Tiwari, S.; Narayan, T.; Jain, U. Bionzymatic assembly formed@Pt nano sensing framework detecting acetylcholine in aqueous phase. *Applied Surface Science*. **2019**, *474*, 154-160, <https://doi.org/10.1016/j.apsusc.2018.04.056>.
40. Jain, U.; Chauhan, N. Glycated hemoglobin detection with electrochemical sensing amplified by gold nanoparticles embedded N-doped graphene nanosheet. *Biosensors and Bioelectronics*. **2017**, *89*, 578-584, <https://doi.org/10.1016/j.bios.2016.02.033>.
41. Palanisamy, S.; Cheemalapati, S.; Chen, S.M. Amperometric glucose biosensor based on glucose oxidase dispersed in multiwalled carbon nanotubes/graphene oxide hybrid biocomposite. *Materials Science and Engineering: C*. **2014**, *34*, 207-213, <https://doi.org/10.1016/j.msec.2013.09.011>.
42. Zaidi, S.A.; Shin, J.H. Recent developments in nanostructure based electrochemical glucose sensors. *Talanta*. **2016**, *149*, 30-42, <https://doi.org/10.1016/j.talanta.2015.11.033>.
43. Cui, F.; Zhou, Z.; Zhou, H.S. Molecularly imprinted polymers and surface imprinted polymers based electrochemical biosensor for infectious diseases. *Sensors*. **2020**, *20*, 996, <https://doi.org/10.3390/s20040996>.

44. Ramanavicius, S.; Jagminas, A.; Ramanavicius, A. Advances in molecularly imprinted polymers based affinity sensors. *Polymers*. **2021**, *13*, 974, <https://doi.org/10.3390/polym13060974>.
45. Sehit, E.; Drzazgowska, J.; Buchenau, D.; Yesildag, C.; Lensen, M.; Altintas, Z. Ultrasensitive nonenzymatic electrochemical glucose sensor based on gold nanoparticles and molecularly imprinted polymers. *Biosensors and Bioelectronics*. **2020**, *165*, 112432, <https://doi.org/10.1016/j.bios.2020.112432>.
46. Canfarotta, F.; Rapini, R.; Piletsky, S. Recent advances in electrochemical sensors based on chiral and nano-sized imprinted polymers. *Current Opinion in Electrochemistry*. **2018**, *7*, 146-152, <https://doi.org/10.1016/j.coelec.2017.11.018>.
47. Yáñez-Sedeño, P.; Campuzano, S.; Pingarrón, J.M. Electrochemical sensors based on magnetic molecularly imprinted polymers: A review. *Analytica chimica acta*. **2017**, *960*, 1-7. <https://doi.org/10.1016/j.aca.2017.01.003>.
48. Yarman, A.; Kurbanoglu, S.; Zebger, I.; Scheller, F.W. Simple and robust: The claims of protein sensing by molecularly imprinted polymers. *Sensors and Actuators B: Chemical*. **2020**, *330*, 129369, <https://doi.org/10.1016/j.snb.2020.129369>.
49. Jain, U.; Soni, S.; Balhara, Y.P.; Khanuja, M.; Chauhan, N. Dual-Layered Nanomaterial-Based Molecular Patterning on Polymer Surface Biomimetic Impedimetric Sensing of a Bliss Molecule, Anandamide Neurotransmitter. *ACS omega*. **2020**, *5*, 10750-10758, <https://doi.org/10.1021/acsomega.0c00285>.
50. Vasapollo, G.; Sole, R.D.; Mergola, L.; Lazzoi, M.R.; Scardino, A.; Scorrano, S.; Mele, G. Molecularly imprinted polymers: present and future prospective. *International journal of molecular sciences*. **2011**, *12*, 5908-5945, <https://doi.org/10.3390/ijms12095908>.
51. Yusof, N.A.; Rahman, S.K.; Hussein, M.Z.; Ibrahim, N.A. Preparation and characterization of molecularly imprinted polymer as SPE sorbent for melamine isolation. *Polymers*. **2013**, *5*, 1215-1228, <https://doi.org/10.3390/polym5041215>.
52. Bing, X.; Wang, G. Label free C-reactive protein detection based on an electrochemical sensor for clinical application. *Int. J. Electrochem. Sci*. **2017**, *12*, 6304-6314, <https://doi.org/10.20964/2017.07.60>.
53. Goda, T.; Toya, M.; Matsumoto, A.; Miyahara, Y. Poly (3, 4-ethylenedioxythiophene) bearing phosphorylcholine groups for metal-free, antibody-free, and low-impedance biosensors specific for C-reactive protein. *ACS applied materials & interfaces*. **2015**, *7*, 27440-277448, <https://doi.org/10.1021/acsami.5b09325>.
54. Thangamuthu, M.; Santschi, C.; JF Martin, O. Label-free electrochemical immunoassay for C-reactive protein. *Biosensors*. **2018**, *8*, 3, <https://doi.org/10.3390/bios8020034>.

**Supplementary material**

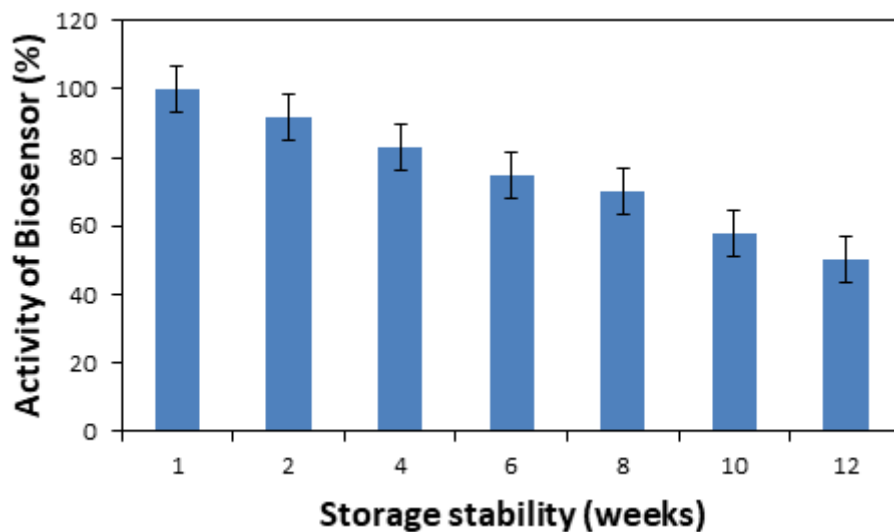


**Figure S1.** Stability of the developed biosensor for 3 months evaluated at every 7<sup>th</sup> day.